The Astrophysical Journal, 890:4 (15pp), 2020 February 10 https://doi.org/10.3847/1538-4357/ab6294

Solitons and Turbulence in Solar Wind at 1 au: Multi-satellite Data and FDTD Simulations

Asif Shah, Saeed-Ur Rehman, Qamar-UL Haque, and Shahzad Mahmood
Theoretical Physics Division (TPD), PINSTECH, P.O. Nilore, Islamabad 44000, Pakistan; masifkf@gmail.com
Received 2019 May 29; revised 2019 December 6; accepted 2019 December 6; published 2020 February 6

Abstract

During 2015 January 1–31 multi-satellite data at 1 au showed the propagation of single soliton pulses, the formation of soliton trains, and their ultimate development into the turbulence in solar wind magnetic field, density, speed, temperature, and dynamic pressure. This work is motivated by a basic research question: what are the differences in the conditions for excitation of soliton pulse, soliton train, and turbulence in the solar wind? To answer this question, a convective and dispersive system is considered and simulated via the finite difference time domain (FDTD) method. It is found that when a system is initially driven by a weak shock wave only a single soliton pulse will propagate. When the convection coefficient is smaller than or equal to the dispersion coefficient and system is driven by a strong shock then soliton trains are formed. The development of turbulence occurs when the convective coefficient dominates the dispersion coefficient and the system is driven by a stronger shock. Combining the findings of FDTD simulations with the Hall magnetohydrodynamic model, it is concluded that an enhanced interplanetary magnetic field in the magnetic sheath and the declining ion density after corotation interaction region interface provide favorable conditions for the solitons formation. Contrarily, the declining magnetic field in ejecta provides pertinent conditions for the evolution of Alfvénic turbulence. Our findings are critical for understanding the wave development into turbulence in solar wind.

Unified Astronomy Thesaurus concepts: Solar wind (1534); Ejecta (453); Corotating streams (314); Shocks (2086); Solar coronal mass ejections (310); Fast solar wind (1872); Fast Fourier transform (1958); Slow solar wind (1873); Interplanetary turbulence (830); Solar storm (1526); Interplanetary physics (827); Alfven waves (23)

1. Introduction

There are many studies about soliton formation in various types of relativistic and nonrelativistic plasma systems comprising electron–ion, electron–positron–ion, multi-ion, negative ions, and dust particles (Berezhiani & Mahajan 1994; Shatashvili et al. 1997; Esirkepov et al. 2002; Lontano et al. 2003; Popel et al. 2003). Contrarily, most of these studies have ignored the initial energy source for exciting solitons in the considered plasma systems. We show that one cannot clearly understand the soliton formation when the initial energy source is ignored. This work applies the finite difference time domain (FDTD) simulations and shows that the formation of single soliton, soliton trains and their breaking is sensitive to the amplitude of initial perturbation, which provides energy for their excitation.

Polar mission and cluster satellites have revealed that magnetic reconnection, two stream, beam-plasma instabilities and electron–ion instabilities can act as energy sources for triggering solitons in the near Earth space (Cattell et al. 2003, 2005; Matsumoto et al. 2003; Graham et al. 2016). The time domain structures (TDS) including electrostatic and electromagnetic electron holes, solitary waves, and double layers are observed by recently launched radiation belt storm probes (twin satellites RBSP-A, RBSP-B; Mozer et al. 2015). The radio and plasma wave science instrument of the *Cassini* mission has confirmed soliton amplitude enhancement due to increased magnetic field inside the Saturn's magnetosphere (Williams et al. 2006). The high frequency electric fields are thought to be driven by plasma turbulence (Stawarz et al. 2015).

The fleet of four cluster spacecraft detected solitons (size of 1000–2000 km and propagating perpendicular to ambient magnetic field at speeds of 250 km s^{-1} with respect to satellite) in the collisionless plasma of the magnetopause boundary. It was found that both temperature and density increased by a factor of 2 and the magnetic field was depressed by 85% (Stasiewicz et al. 2003). Geostationary satellites *GOES* 5, 3, and 2 have detected 292 events of soliton formation inside Earth's magnetosphere during 1979–1984. However, 184 events showed propagation parallel and perpendicular with respect to ambient magnetic field. It was also found that solitary waves become unstable beyond a critical range of wave numbers (Patel & Dasgupta 1987). Stasiewicz (2004) studied magnetosonic structures in the magnetosheath region under varying conditions of plasma beta (ratio of kinetic to magnetic pressure). Pokhotelov et al. (1996) discussed the Alfvén solitons and magnetosonic solitons propagating along the lines of geomagnetic field for various cases of propagation angles. Their results were applied to explain soliton formation during Russian seismic impact experiments. Fränz et al. (2003) discussed the solitary wave formation in the solar wind. Ovenden et al. (1983) obtained the turbulence spectrum resulting from piling up of solitons in the presence of circularly polarized Alfvén oscillations and high speed solar wind streams.

The soliton formation requires a balance between convection and dispersion. However, the standard magnetohydrodynamic (MHD) does not give any dispersive effects in an ideal long wave length limit. But the dispersion in magnetized plasma is introduced by the assumption of finite wave length oscillations when the Hall term is retained in the generalized Ohm's law. In warm plasma, dispersion effects arise due to finite ion gyro-radius and anisotropic electron pressure (Mjolhus & Hada 1997). It has been found that shock nonstationarity and reformation are triggered by magnetosonic soliton conversion

into shocks (Gueroult et al. 2017). The nonlinear magnetosonic pulses can lead to particle reflection along the magnetic field via two types of mechanisms. Basically, in compressive solitons, with their intensified magnetic field, electrons characterized by large magnetic moments can be reflected by the magnetic mirror effect. However, in rarefactive solitons with weaker magnetic field (smaller than outside) electrons with smaller magnetic moment can be reflected by parallel Pseudo potential (Ohsawa 2017). Recently, it has been discovered that the magnitude of parallel pseudo potential of the shock wave along magnetic field line depends on wave amplitude, kinetic energy of the ion, and electron temperature (Ohsawa 2018). The energy transfer to heavy ions in the presence of external magnetic field also leads to magnetosonic solitons (Kumar et al. 2019).

Turbulence is basically a transient state between order and disorder (Treumann & Baumjohann 1997). A large number of studies have focused on various aspects (wave steepening caused mode pile up, phase mixing, energy cascading, excitation of microinstabilities, associated particle transport, and diffusion, plasma stability etc.) of solar wind turbulence (Goldstein et al. 1995; Goldstein & Roberts 1999; Goldstein 2001). The MHD turbulence is a broadband nonlinear dynamical interaction of fluctuating quantities (e.g., magnetic field, pressure, density, and speed) in solar wind plasma. It leads to strong coupling across multiple spatial and temporal scales. The turbulent coupling also leads to energy exchange among modes. The strong gradients in flow speeds (when slow and fast solar wind streams mutually interact) is one of the reasons for turbulence evolution in solar wind plasma (Yoshizawa et al. 2002; Burch et al. 2004; Boozer 2005). However, turbulence in this work is caused by nonlinear waves piling up due to high convection in solar wind plasma (as explained in Goldstein et al. 1995; Burch et al. 2004).

The solar wind sometimes contains coronal mass ejections (CME) or substructures of CME (shocks, sheaths, and magnetic cloud (MC)), complex ejecta, corotation interaction region (CIR), and heliospheric current sheets. The CMEs are large plasma and magnetic field eruptions from solar corona traveling at a variety of speeds (a few hundred to thousands of kilometers per second). At large distances away from the Sun, a CME is termed as an interplanetary coronal mass ejection (ICME; Howard 2011). The sheath and CIR are driven by different processes. When a fast CME/ICME overtakes a slow plasma volume then a compression region called a sheath is formed, where density, temperature, and magnetic field are increased almost simultaneously, sometimes shocks are also formed at the leading edge of the sheath (Yermolaev et al. 2009, 2017). When there is a large velocity gradient then the fast solar wind stream plays the role of a piston and leads to the formation of CIRs. In CIRs both the density and interplanetary magnetic field (IMF) increase before an increase in the temperature, and solar wind streaming speed (Hutchinson et al. 2011).

The MC and ejecta are substructures of CMEs and are characterized by stronger magnetic fields. The MC is characterized by a more slowly varying smoother magnetic field (Burlaga et al. 1981). Studies have shown that MC structure exists in the presence of single CME but ejecta can be due to multiple sources, e.g., resulting from the interaction of two or more CMEs. It has been found that successive CMEs can merge together in the interplanetary space and give rise to the formation of ejecta. However, sometimes the situation can become complex when multiple corotation regions and CMEs mutually interact. Such a merging is a nonlinear process and one cannot clearly separate various large scale structures merged together in an ejecta (Burlaga et al. 2002). Many studies have focused on the large scale structures in solar wind (for example, Burlaga et al. 1981; Gonzalez & Tsurutani 1987; Hundhausen et al. 1994; Gosling & Pizzo 1999; Richardson et al. 2000; Tsurutani et al. 2004; Koskinen & Huttunen 2006; Echer et al. 2008; Jian et al. 2008; Richardson & Cane 2011; Kilpua et al. 2017a, 2017b).

The large scale structures in solar wind drive geomagnetic storms which represent significantly disturbed geomagnetic field (Gonzalez et al. 1994) and can be described in terms of disturbance storm time (Dst) index. The storms can have three phases: sudden storm commencement (SSC phase; positive Dst value due to the compression of magnetosphere by interplanetary shock), initial phase (interval of unchanging Dst after SSC), and main phase (Dst becomes negative and declines with time. Dungey (1961) suggested that the main phase of a storm is caused by magnetic reconnection of IMF and Earth's magnetic field, which transfers energy from solar wind to geomagnetosphere. The energy transfer occurs efficiently when IMF is southward directed or points opposite to the Earth's magnetic field) and recovery phase (recovers Dst to its pre-storm value due to the decay of the ring current) (Koskinen 2011).

There are many observations of nonlinear wave formation in the near Earth space. However, for developing detailed understanding of nonlinear waves in space, it is important to link satellite observations with numerical simulations. Therefore, this work is focused on FDTD simulations to explain the satellite observations during 2015 January 1–31. The manuscript is organized as follows: Section 2 elaborates on the FDTD algorithm. Section 3 presents the multi-satellite observations at 1 au based on the OMNI data. Section 4 explains CIRs and CME components. FDTD simulation results are described in Section 5. Section 6 is devoted to discussion. Section 7 presents a summary and conclusions.

2. Numerical Algorithm

This work uses the Korteweg–de Vries (KdV) equation (De Vries & Korteweg 1895; Belashov & Vladimirov 2005),

$$\partial_t \phi + A\phi\partial_x \phi + B\partial_x^3 \phi = 0 \quad (1)$$

in normalized form to simulate and study nonlinear waves in the solar wind plasma. Here A and B are the convection and dispersion coefficients respectively. Coefficient A gives rise to wave steepening and breaking. Contrarily, coefficient B is responsible for dispersion and wave spreading. Equation (1) can pertinently model nonlinear waves in magnetohydrodynamics, plasma physics, and theory of lattices and many other physical systems with dispersive and convective effects (Belashov & Vladimirov 2005). This work avoids the stationary solution and applies the following FDTD method (Taflove & Hagness 2005) to study the temporal evolution of the nonlinear waves under varying initial conditions and different ratios of coefficients A and B. Using the FDTD scheme, one can approximate the time derivative in the first

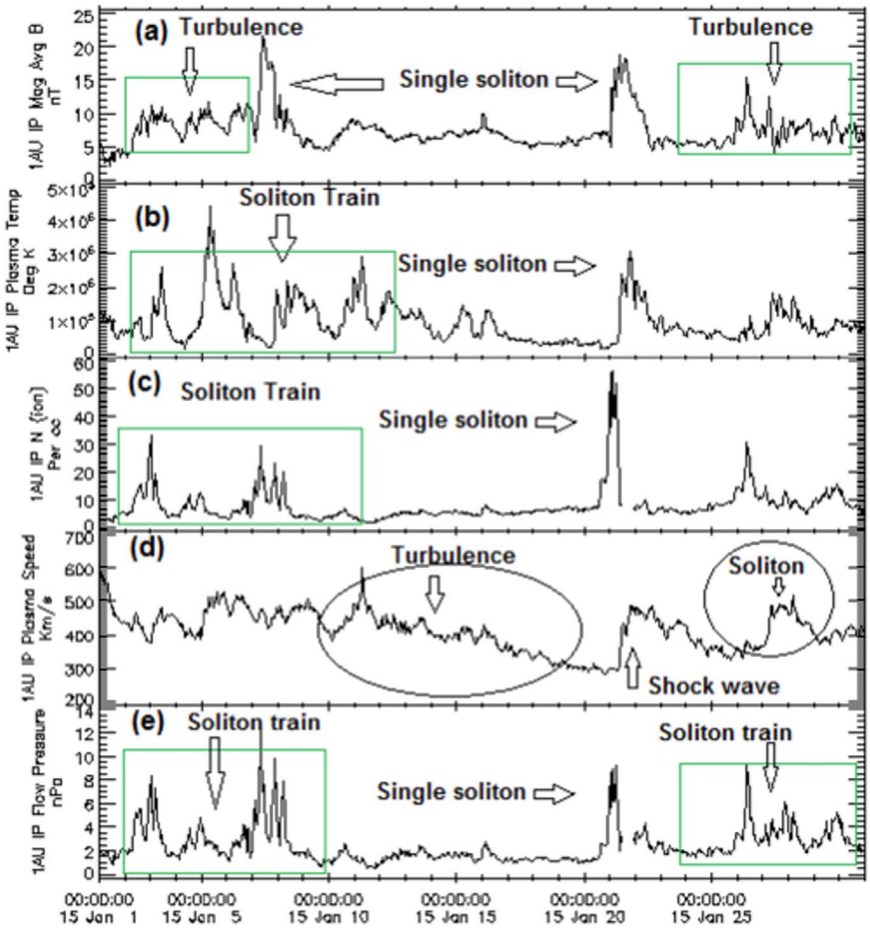

Figure 1. Single soliton and soliton trains and turbulence in (a) interplanetary magnetic field, (b) solar wind plasma temperature, (c) solar wind density, (d) solar wind plasma speed, and (e) dynamic pressure observed by multi-satellites associated with OMNI data during 2015 January 1–31.

term of Equation (1) as (Taflove & Hagness 2005),

$$\partial_t \phi = \frac{\phi(x, t + \Delta t) - \phi(x, t - \Delta t)}{2\Delta t}. \quad (2)$$

Equation (2) is based on the central difference centered at t. Equation (2) in the simplified form appears as,

$$\partial_t \phi = \frac{\phi_{i,j+1} - \phi_{i,j-1}}{2\Delta t}. \quad (3)$$

The space grid is incorporated as $x = i\Delta x$ and time runs as $t = j\Delta t$. Here Δx, Δt represent the space and time steps respectively. The space derivative in the second term of Equation (1) can be approximated as,

$$\partial_x \phi = \frac{\phi_{i+1,j} - \phi_{i-1,j}}{2\Delta x}. \quad (4)$$

Similarly, to determine the $\partial_x^3 \phi$, the $\phi(x, t)$ is expanded about four points $\phi(x \mp 2\Delta x, t)$ and $\phi(x \mp \Delta x, t)$. This gives,

$$\phi(x \mp \Delta x, t) = \phi(x, t) \mp \Delta x(\partial_x \phi) \mp \frac{(\Delta x)^2}{2!}\partial_x{}^2 \phi \mp \frac{(\Delta x)^3}{3!}\partial_x{}^3 \phi. \quad (5)$$

One can determine a similar expansion for $\phi(x \mp 2\Delta x, t)$, use these expansions in Equation (1), and obtain the following algorithm,

$$\phi_{i,j+1} = \phi_{i,j-1} - \frac{A\Delta t}{3\Delta x}(\phi_{i+1,j} + \phi_{i,j} + \phi_{i-1,j})(\phi_{i+1,j} - \phi_{i-1,j}) - \frac{B\Delta t}{(\Delta x)^3}(\phi_{i+2,j} + 2\phi_{i-1,j} - 2\phi_{i+1,j} - \phi_{i-2,j}). \quad (6)$$

Equation (6) gives the future value $\phi_{i,j+1}$ which is dependent on the present solutions (terms with the index j) and past solutions (terms with index $j-1$). The solitons are initiated by driving the system by a shock wave initially at time $t = 0$,

$$\phi(x, t = 0) = \phi_0\left(1 - \tanh\left(\frac{x - 25}{5}\right)\right). \quad (7)$$

3. Single Soliton, Soliton Trains, and Turbulence in Solar Wind at 1 au

This work utilizes multisource data sets as extracted from NASA/GSFC's OMNI data set through OMNIWeb (https://omniweb.gsfc.nasa.gov). We use one hour resolution merged data of IMF, ion number density, plasma flow speed, dynamic pressure, and temperature. Figure 1 exhibits solitons and turbulence in the solar wind at 1 au during 2015 January 1–31. In Figure 1(a) the regions enclosed by green rectangles indicate turbulence (different frequencies mixed together) in the IMF.

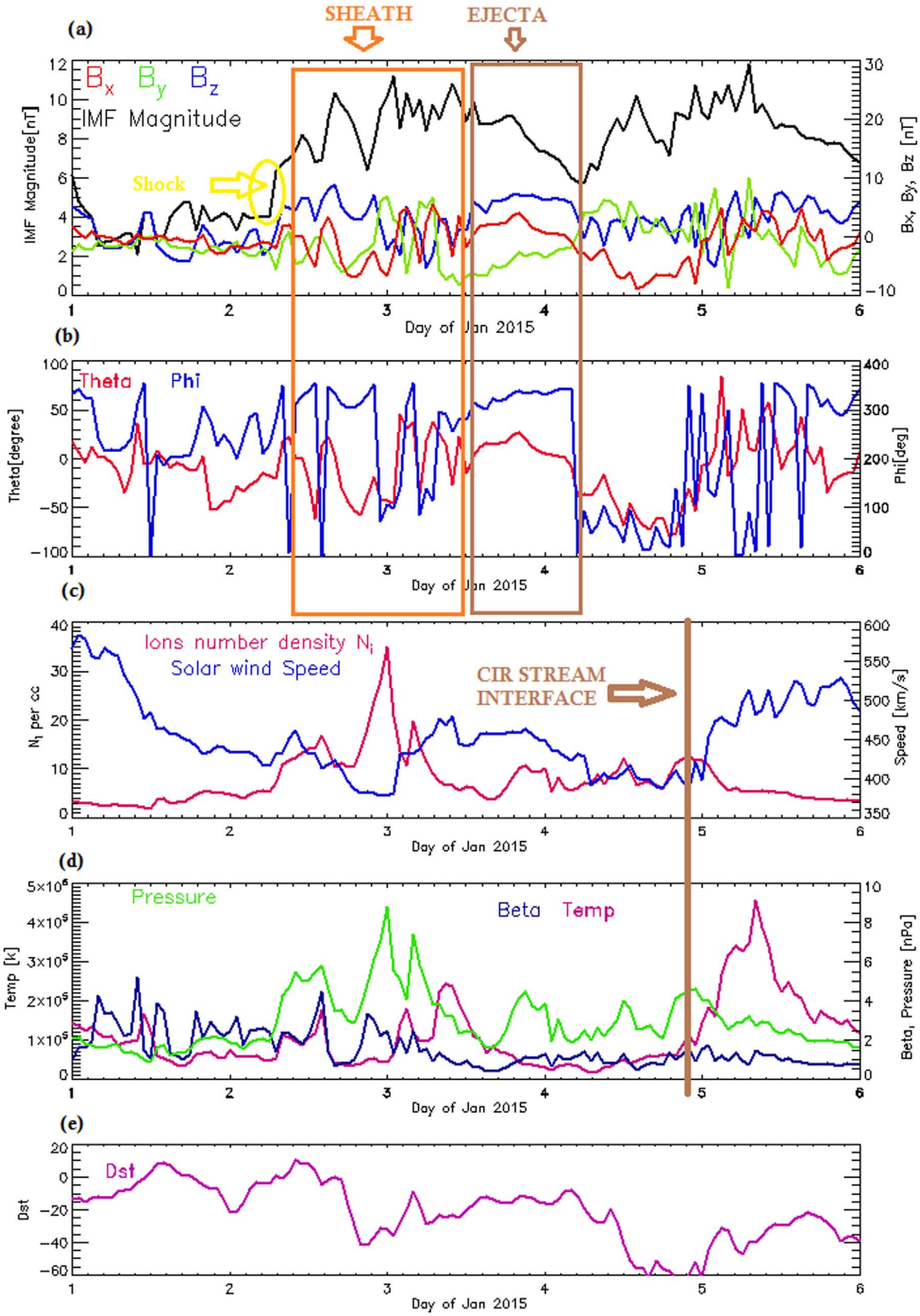

Figure 2. Shock, sheath, ejecta, and CIR in solar wind during 2015 January 1–6.

Two solitons are also obvious in the IMF. Figure 1(b) displays the soliton trains in the plasma temperature. The soliton train is made up of solitons characterized by unequal amplitudes. Later on a single soliton appears which is followed by turbulence in temperature. The plasma density also exhibited various types of nonlinear structures, as shown in Figure 1(c). The initial soliton

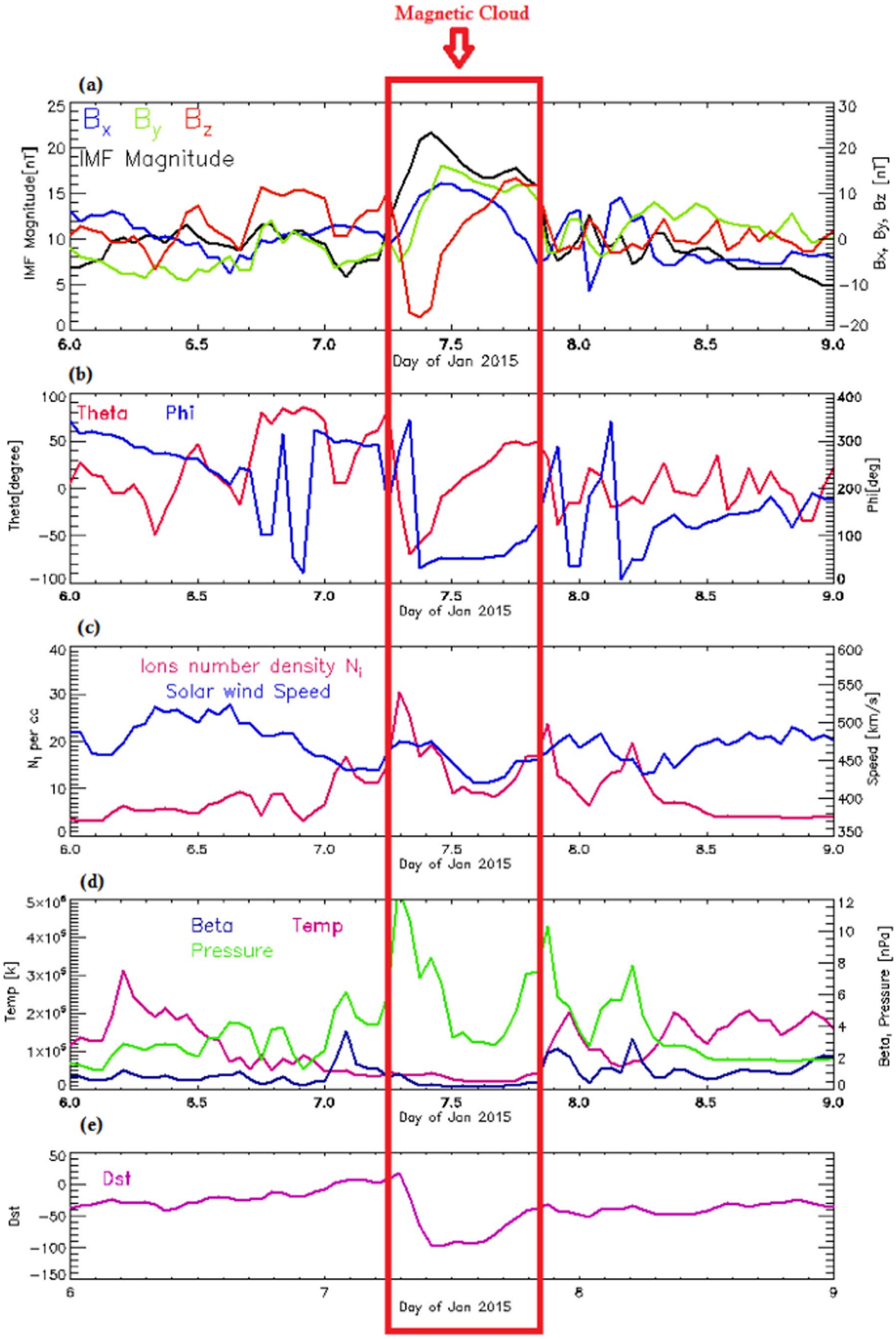

Figure 3. Magnetic cloud (MC) in solar wind during 2015 January 6–9.

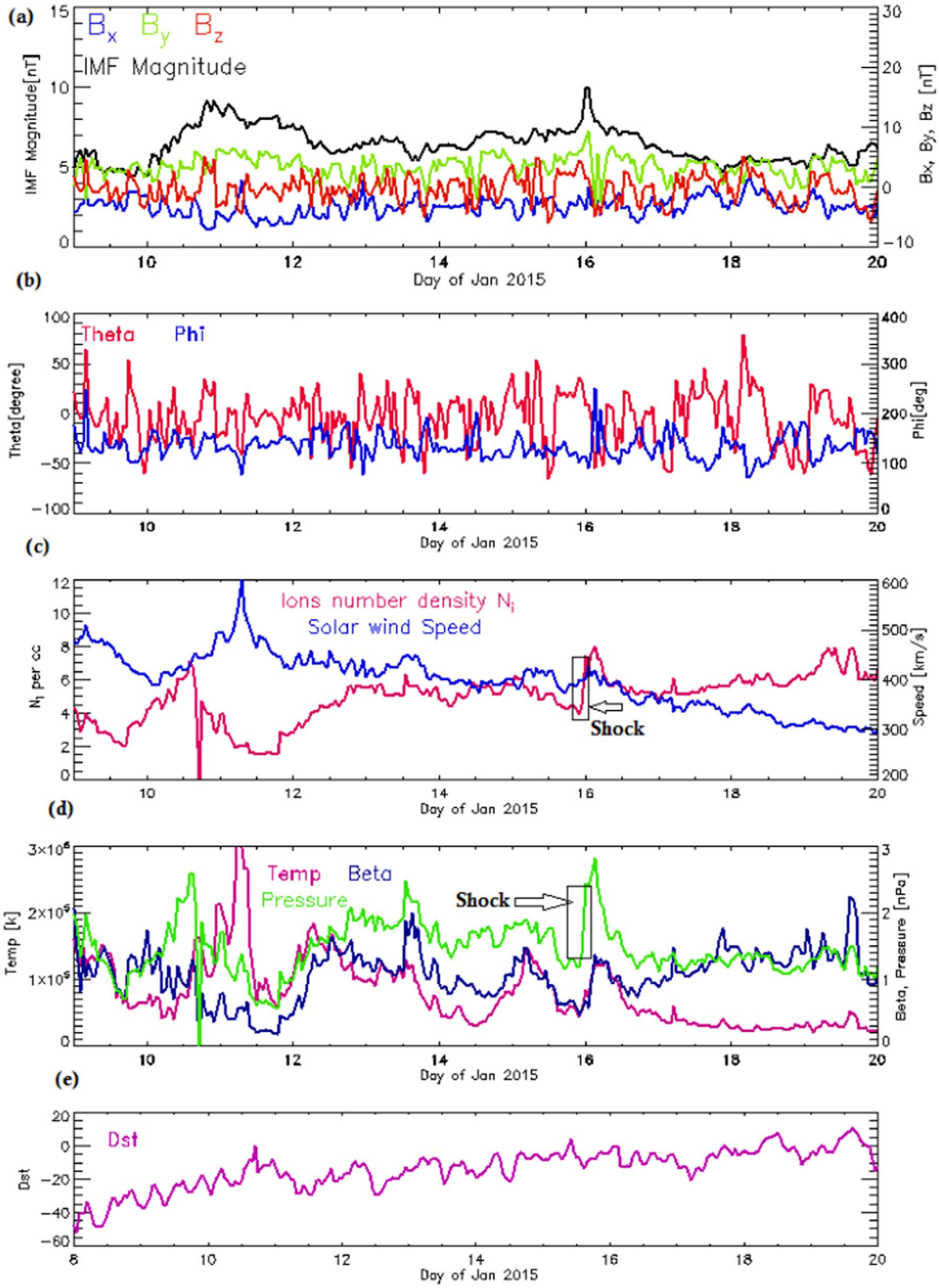

Figure 4. Shocks in solar wind during 2015 January 9–20.

train is followed by a high amplitude single soliton, and then there are two further solitons with diminishing amplitudes. Figure 1(d) shows the occurrence of solitons, shock, and turbulence in the solar wind speed. The solar wind dynamic pressure also showed single as well as soliton trains comprising components with varying amplitudes.

The appearance of solitons and turbulence in different solar wind parameters at the same time (in Figure 1) indicates that the dynamics of considered parameters are mutually coupled in the following manner. The shock compresses both magnetic field and density in the presence of speed gradients. The dynamic pressure ($=nmV^2$, where n is number density, m is

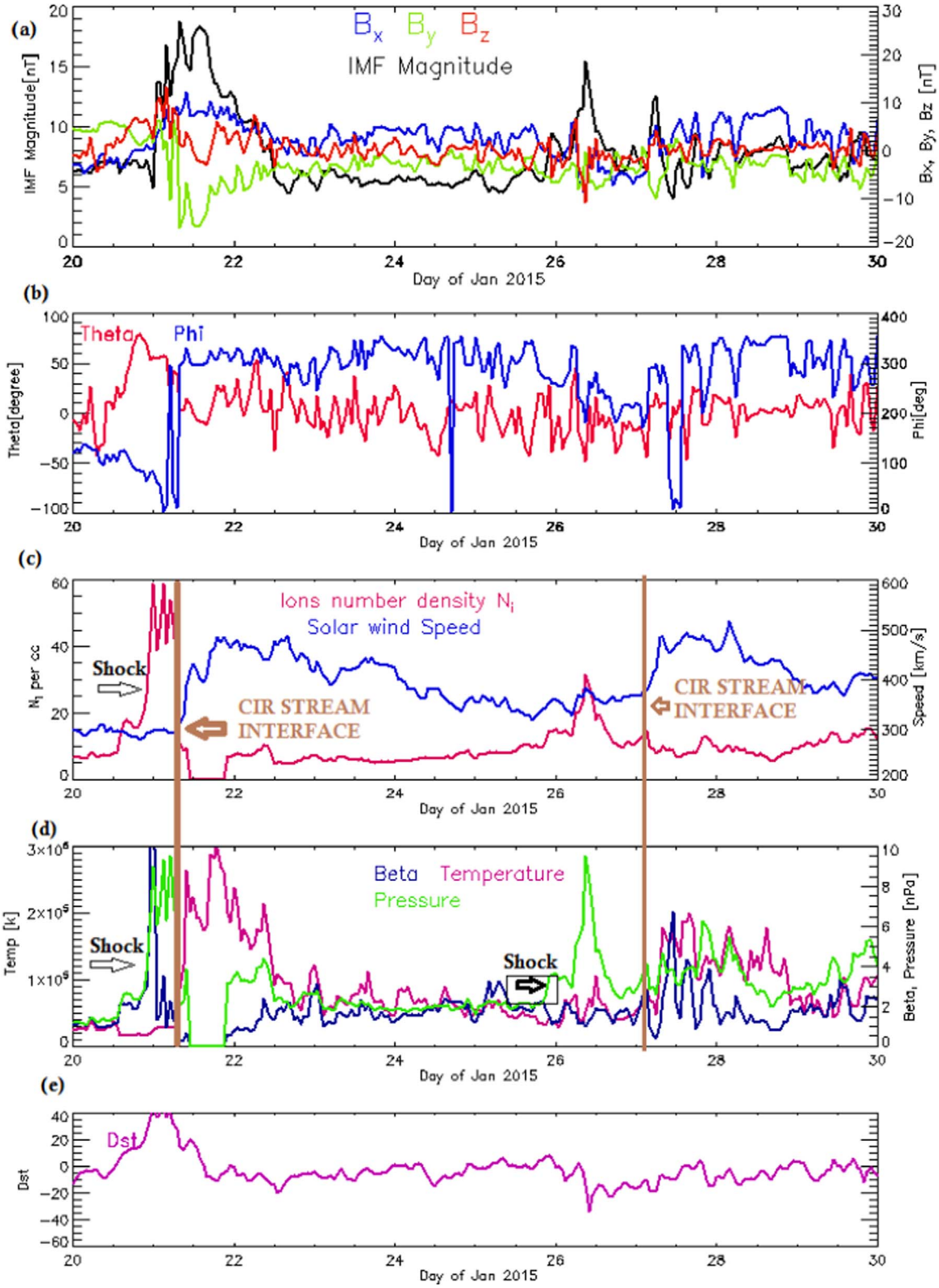

Figure 5. Shocks and CIRs in solar wind during 2015 January 20–30.

mass, and V is speed) depends on the mass, ions number density, plasma flow speed. Therefore, the oscillations in both speed and density are coupled with pressure and induce oscillations in pressure. This study explains the soliton train's formation and turbulence via finite difference time domain (FDTD) simulations.

4. CME and CIR as Energy Sources of Solitons and Turbulence

Figure 2 presents solar wind data during 2015 January 1–6. The three components of a CME (comprising shock, sheath, and ejecta) are highlighted during 2.3–4.2 January. The shock

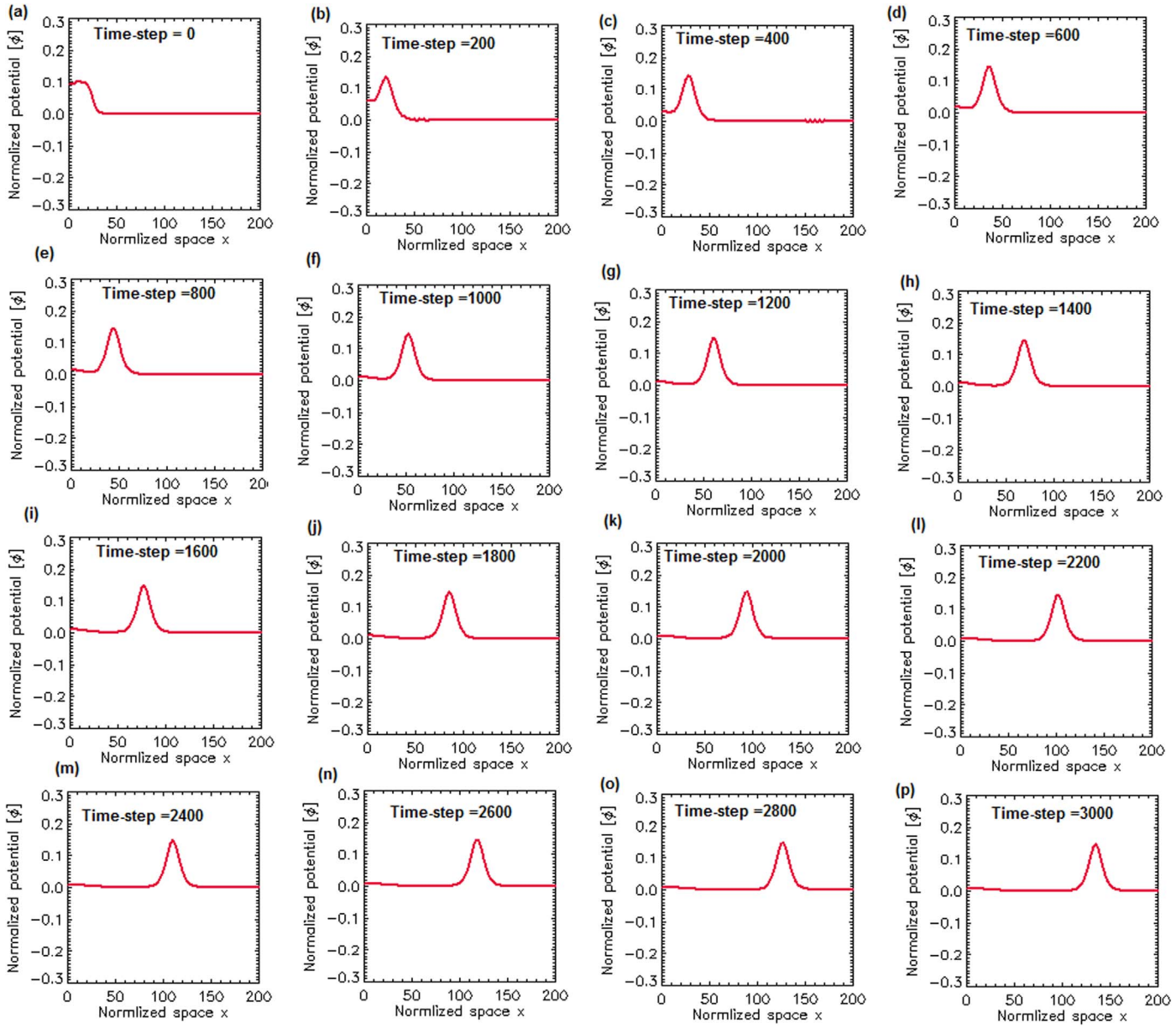

Figure 6. Simulations of single soliton propagation. The other parameters are $A = 0.85$, $B = 0.85$, $dt = 1$, $dx = 2.5$, and $\phi_0 = 0.05$.

is a jump in IMF, highlighted by a yellow circle. The shock is followed by sheath which is highlighted by an orange rectangular region. In sheath the IMF is significantly higher than IMF values before CME shock arrival. During sheath, ion number density (Figure 2(c)) and solar wind dynamic pressure (Figure 2(d)) also simultaneously increased with IMF enhancement. The sheath is followed by ejecta, enclosed in a different rectangle. Basically, the IMF (black curve Figure 2(a)), its components (B_x, B_y, and B_z in Figure 2(a)), IMF latitude (theta, Figure 2(b)), and longitude (phi, Figure 2(b)) angles in ejecta are smoother than these quantities in sheath. In ejecta, temperature, and plasma beta (Figure 2(d)) are decreasing. From the disturbance storm time (Dst) index given in Figure 2(e), one can compare the effects of sheath and ejecta on the Earth's magnetosphere. The Dst (Figure 2(e)) dip during sheath is deeper than Dst dip during ejecta. Therefore, the sheath was more geoeffective than ejecta. The position of CIR interface is highlighted by a thick vertical line at 4.9 January in Figures 2(c) and (d). Toward the right of stream interface density and pressure were declining but solar wind speed (Figure 2(c)) and temperature (Figure 2(d)) increased.

Figure 3 shows solar wind parameters during 2015 January 6–9. An MC is enclosed inside a red rectangular region. In MC IMF and its components (B_x, B_y, B_z in Figure 3(a)) are significantly stronger, smoother. The latitude and longitude (theta and phi) angles are slowly varying in MC and speed, density, pressure, temperature, and plasma beta were all decreasing with time. The Dst-dip in Figure 3(e) indicates that MC in Figure 3 was more geoeffective than sheath in Figure 2. The solar wind data during 2015 January 9–20 is shown in Figure 4. The shocks in ion number density (Figure 4(c)) and dynamic pressure (Figure 4(d)) on January 15 are highlighted. Most of the time IMF (Figure 4(a)) was less than 9 nT and IMF components, speed, density, and pressure show rapid oscillations riding on top of slowly varying trends, which indicates the presence of turbulence in the solar wind. The solar wind

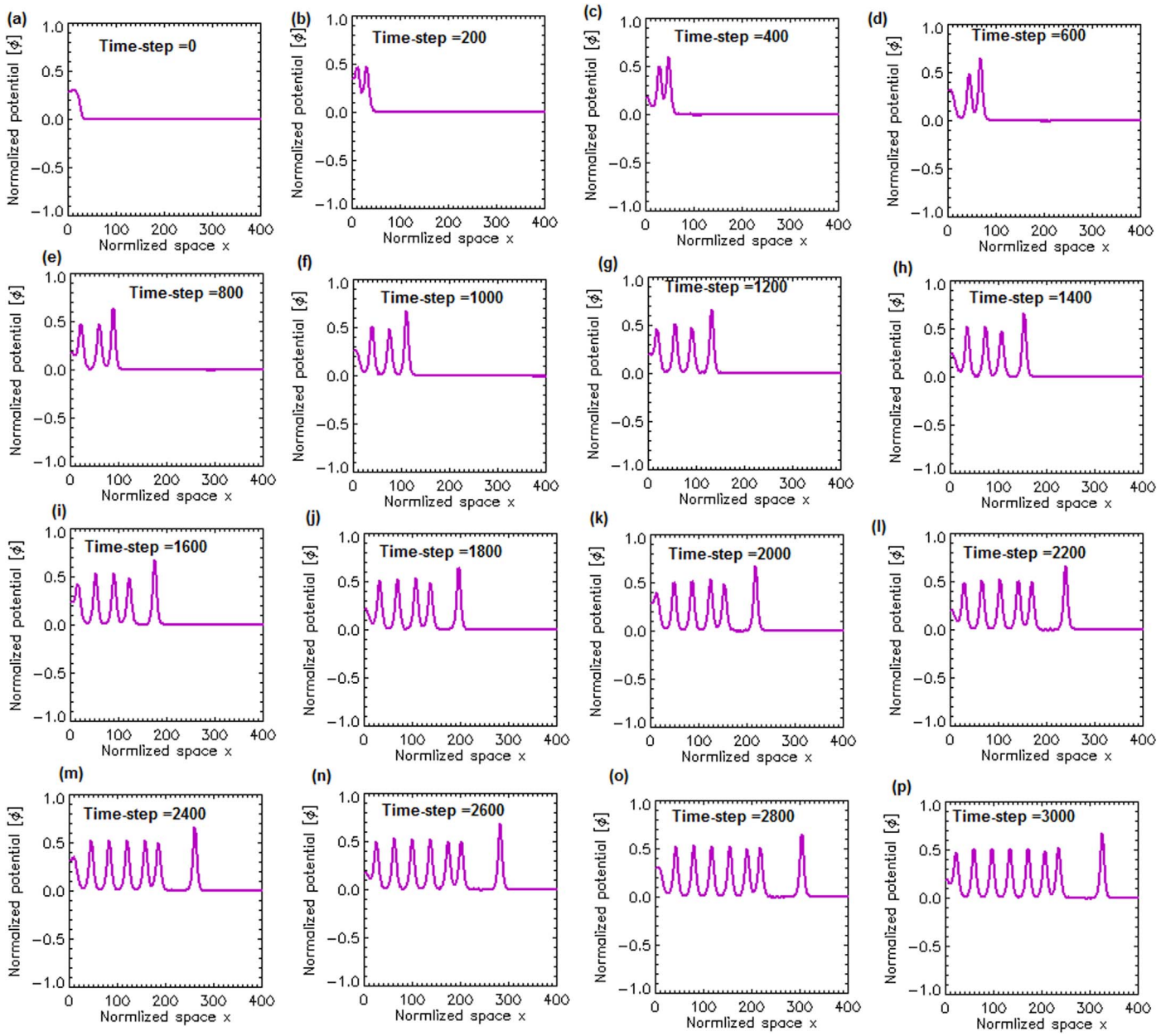

Figure 7. Simulations of soliton train propagation. The other parameters are $A = 0.5$, $B = 0.75$, $dt = 1$, $dx = 2.5$, and $\phi_0 = 0.15$.

plasma and magnetic field parameters during 2015 January 20–30 are presented in Figure 5. There are two CIRs. The stream interface for first CIR is highlighted with a vertical line on January 21 in Figures 5(c) and (d). Before this a strong shock appeared which increased ion number density beyond 40 cm^{-3} and pressure (Figure 5(d)) peaked almost at 8 nPa. On January 26, IMF increased and in the same interval solitons formed in density (Figure 5(c)) and dynamic pressure (Figure 5(d)). The stream interface of second CIR is highlighted on January 27.

The soliton formation and turbulence occurred after or during CME and CIRs. Therefore, from Figures 1–5 one can interpret that soliton excitation, soliton train formation, and evolution into turbulence are energized and excited by shocks, CME components (sheath, MC, and ejecta), and CIRs. Further details and comparisons with model and simulations are provided in the discussion section.

5. Simulation Results

Figure 6 shows the propagation of single soliton for a very high value of nonlinear convection coefficient (A) in the system. But the dispersion coefficient (B) is also high and tantamount ($A = B = 0.85$) to the nonlinear convection coefficient. The weak shock wave ($\phi_0 = 0.05$) provides the initial energy for triggering waves in the considered convective and dispersive system modeled by Equation (1). For Figure 7, the ratio of B/A is 1.5 and the difference B–A is 0.25 but the system is driven initially by a stronger shock wave ($\phi_0 = 0.15$). At time step = 0 only a shock driver is evident. At time step = 400 almost two solitons are formed. The number of solitons are increasing with time and at time step =2800 a soliton train of seven solitons is formed in the system. For Figure 8 the initial shock driver is further strengthened ($\phi_0 = 0.25$). But the ratio $B/A = 5$ and difference B–A is 0.6. Initially at time step = 0, only the shock driver can be seen in

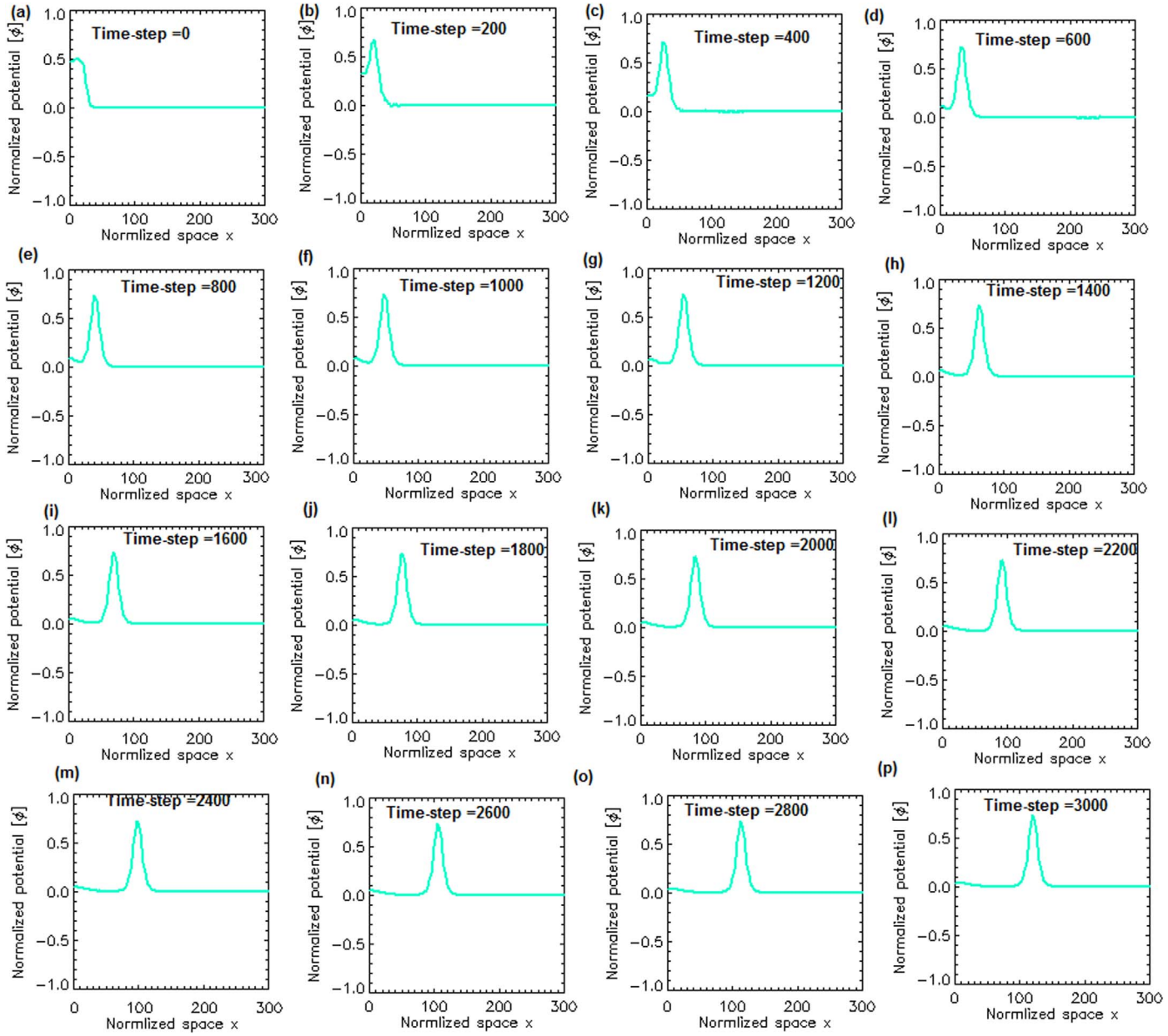

Figure 8. Simulations of single soliton propagation. The other parameters are $A = 0.15$, $B = 0.75$, $dt = 1$, $dx = 2.5$, and $\phi_0 = 0.25$.

Figure 8(a). This shock develops into a soliton and there is no multiplication of solitons with time in spite of driving the system by a stronger shock wave. For Figure 9, the initial shock strength ($\phi_0 = 0.15$) is equal to that used for Figure 7. But now the ratio B/A is 0.75 and the difference B–A is—0.05. Figure 9 shows that initial shock leads to turbulence in the considered system. For Figure 10 the ratio of B/A is unity and the difference B–A is null, similar to the case used for Figure 6. But for Figure 10 the initial shock driver strength is equal to Figure 9 and is much stronger than that used for Figure 6. One can see from Figure 10 that the shock driven system develops a soliton train with the passage of time.

6. Discussion

To explain the simulation results (Figures 6–10) and multi-satellite observations (Figures 1–5) and link them with each other, this work considers the Hall MHD model governed by the following equations (Ballai et al. 2003),

$$\frac{\Delta\rho}{\partial t} + \nabla \cdot (\rho \boldsymbol{v}) = 0 \tag{8}$$

$$\rho\left[\frac{\partial \boldsymbol{v}}{\partial t} + \boldsymbol{v} \cdot \nabla \boldsymbol{v}\right] + \nabla p - \frac{1}{\mu_0}[(\nabla \times \boldsymbol{B}) \times \boldsymbol{B}] = 0 \tag{9}$$

$$\frac{\partial \boldsymbol{B}}{\partial t} - \nabla \times (\boldsymbol{v} \times \boldsymbol{B}) - \frac{m_i}{e\rho\mu_0}(\boldsymbol{B} \cdot \nabla)\nabla \times \boldsymbol{B} = 0 \tag{10}$$

$$\left[\frac{\partial}{\partial t} + \boldsymbol{v} \cdot \nabla\right](p\rho^{-\gamma}) = 0. \tag{11}$$

Here ρ, v, p, γ, B, e, and m_i represent mass density, flow velocity, pressure, adiabatic index, magnetic induction vector, electron charge, and ion mass respectively. Using the perturbation techniques one can arrive at the following KdV

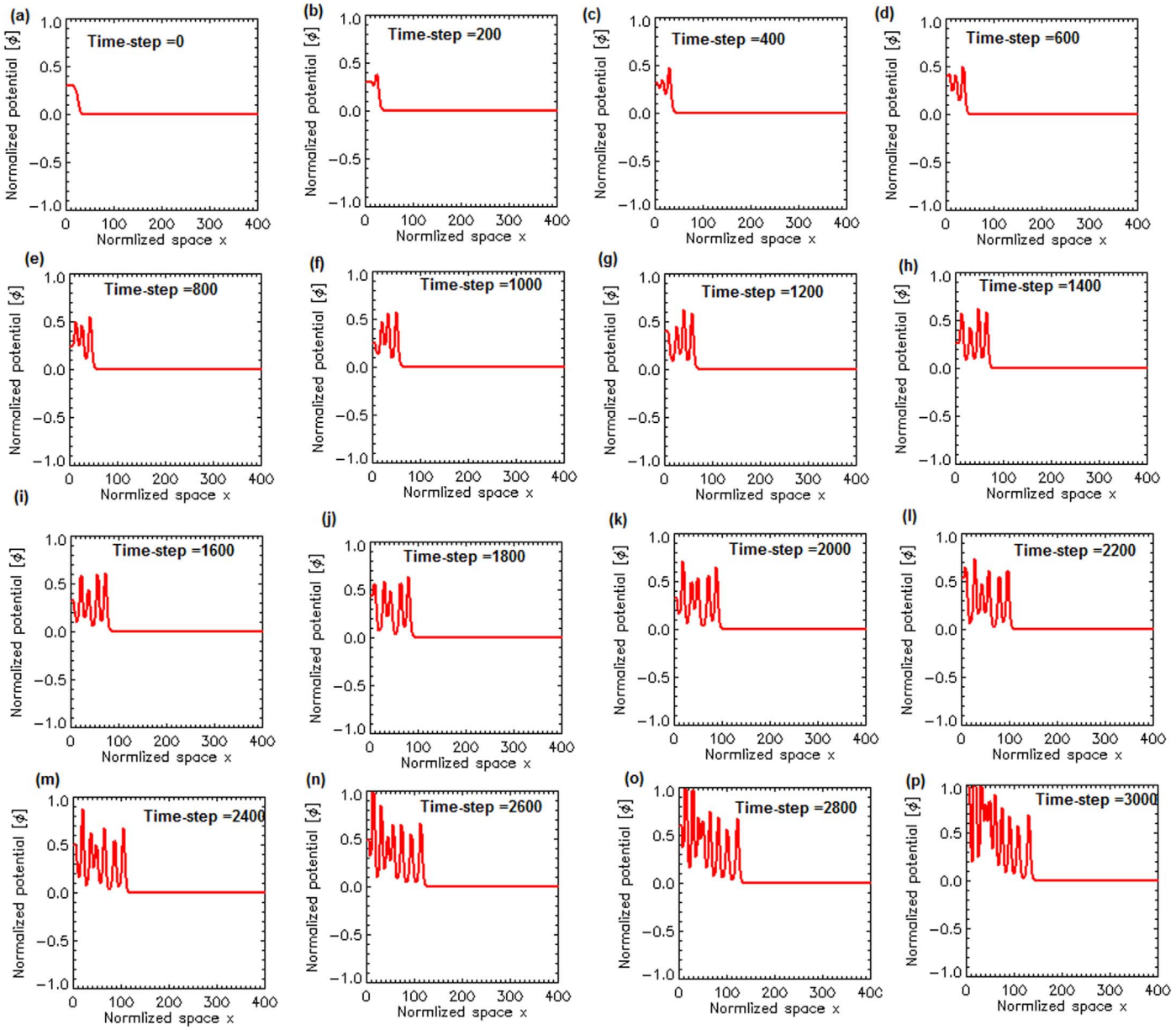

Figure 9. Simulations of soliton evolution into turbulence. The other parameters are $A = 0.2$, $B = 0.15$, $dt = 1$, $dx = 2.5$, and $\phi_0 = 0.15$.

equation for perturbed pressure (p^1) (Ballai et al. 2003),

$$\frac{\partial p^1}{\partial \tau} + Ap^1 \frac{\partial p^1}{\partial \xi} + B\frac{\partial^3 p^1}{\partial \xi^3} = 0. \tag{12}$$

Here convection coefficient (A) and dispersion coefficient (B) read as,

$$A = \frac{V_{f,s}[c_s^2(1+\gamma)(V_{f,s}^2 - V_a^2\cos^2\alpha) + 3V_{f,s}^2(V_{f,s}^2 - c_s^2)]}{2c_s^2\rho_0(2V_{f,s}^4 - c_s^2V_a^2\cos^2\alpha)} \tag{13}$$

$$B = \frac{V_a^4\cos^2\alpha V_{f,s}^3(V_{f,s}^2 - c_s^2)}{2\omega_i^2(2V_{f,s}^4 - c_s^2V_a^2\cos^2\alpha)(V_{f,s}^2 - V_a^2\cos^2\alpha)} \tag{14}$$

The phase speeds of fast (V_f) and slow (V_s) magnetosonic waves read as,

$$V_{f,s} = \sqrt{\frac{c_s^2 + V_a^2 \pm \sqrt{c_s^4 + V_a^4 - 2c_s^2V_a^2\cos 2\alpha}}{2}}. \tag{15}$$

The sound speed $c_s = \sqrt{\gamma p_0/\rho_0}$ and Alfvén speed $V_a = B_0/\sqrt{\mu_0\rho_0}$. The quantities with subscript 0 indicate equilibrium (ρ_0, p_0) values and B_0 is ambient magnetic field and μ_0 represents the permeability of free space. The symbol α represents the wave propagation angle with respect to B_0.

The effects of solar wind parameters on the ratio of coefficients A/B (given by Equations (6) and (7)) for fast magnetosonic wave are presented in Figure 11. For instance, the effects of IMF on A/B are shown in Figure 11(a). When IMF < 5 nT, then $A \gg B$ and the ratio A/B (blue curve) is not matched with critical balance (shown by a flat green line when

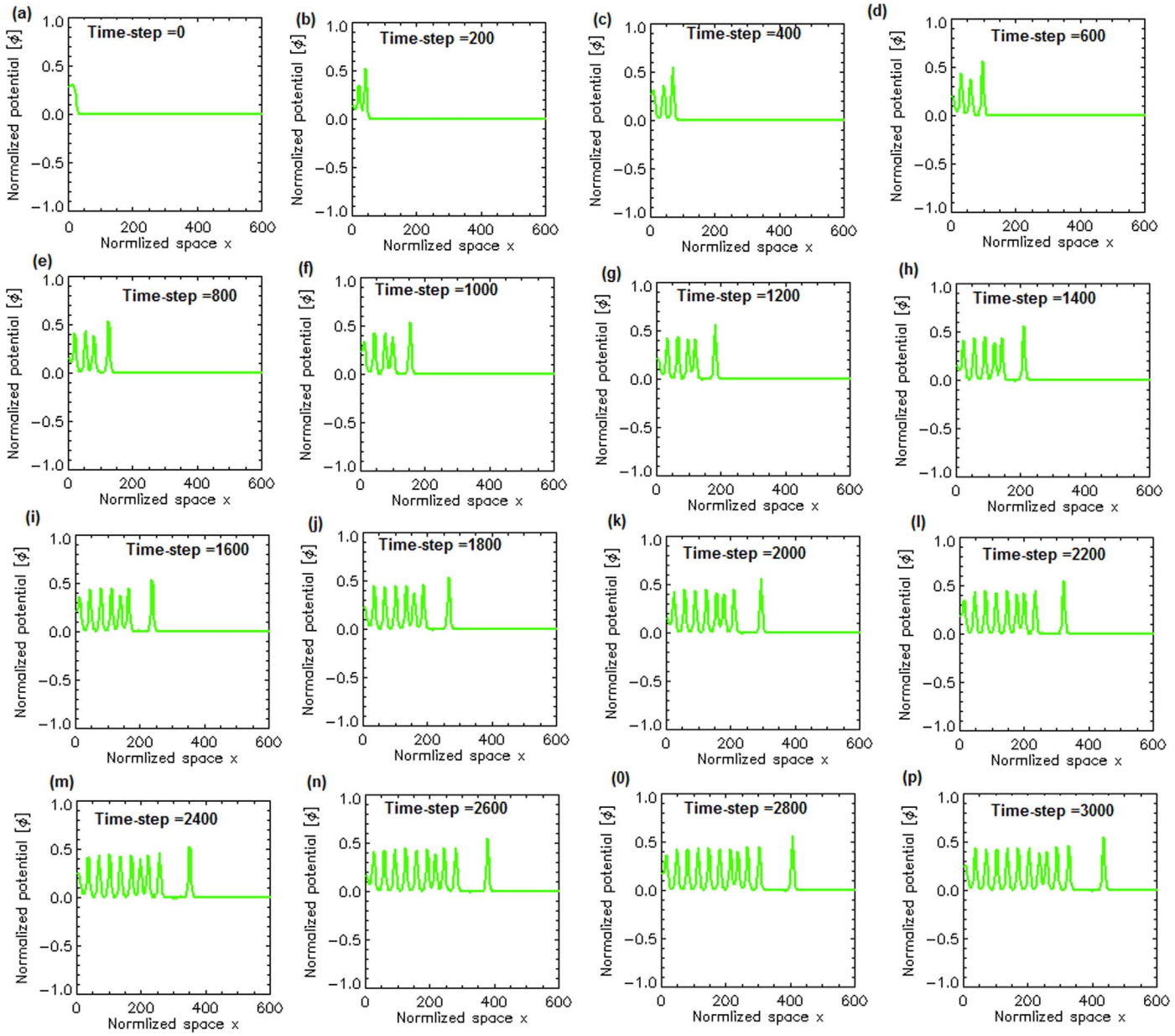

Figure 10. Simulations of soliton train propagation. The other parameters are $A = 0.8$, $B = 0.8$, $dt = 1$, $dx = 2.5$, and $\phi_0 = 0.15$.

$A = B$) condition for soliton formation. However, when IMF is increasing from 5 to 8 nT then A/B ratio (blue curve) approaches a critical level (flat green line). For IMF > 9 nT, the blue curve overlaps the green line. Therefore, one can argue that convection coefficient increases with the decrease of IMF. Contrarily, the increase of magnetic field leads to an enhancement in the dispersion coefficient. Consequently, one can expect the formation of soliton pulses and soliton trains at high magnetic field. Contrarily, the development of turbulence should be expected at weak magnetic field. These predictions are in good agreement with multi-satellite solar wind data presented in Figures 1–5. For example, during 2.5–3.5 January (Figure 2), when IMF (black curve in Figure 2(a)) is high in magnetic sheath, then soliton pulse is obvious in the ion number density (Figure 2(c)) and soliton trains appear in dynamic pressure (Figure 2(d)). Similarly, the turbulence can be seen in the solar wind speed and density (Figure 4(c)), as well as in dynamic pressure and proton temperature (Figure 4(d)) during 2015 January 12–14, when IMF is less than 7 nT, these quantities show turbulent rapid oscillations.

Figure 11(b) shows the effects of ion number density (n_i) on the ratio of convection to dispersion coefficients (A/B given by Equations (6) and (7)). When $n_i < 8\,\mathrm{cm}^{-3}$, then $A < B$ and dispersion coefficient (B) dominates the convection coefficient (A). In this limit, a strong shock will possibly be able to excite soliton trains. However, for a critical density domain when $9\,\mathrm{cm}^{-3} < n_i < 10\ \mathrm{cm}^{-3}$ then convection coefficient (A) becomes comparable to dispersion coefficient (B) and one can expect soliton formation to occur. Contrarily, when $n_i > 11\ \mathrm{cm}^{-3}$ then $A/B \gg 1$, wave steepening due to convection cannot be balanced by weaker dispersion. This can lead to wave energy cascading and turbulence in solar wind.

The effect of proton temperatures (T_p) on the ratio A/B is presented in Figure 11(c). When proton temperature $T_p < 2 \times 10^5$ K, the convection coefficient (A) is balanced by dispersion coefficient (B) and ratio A/B becomes one, which

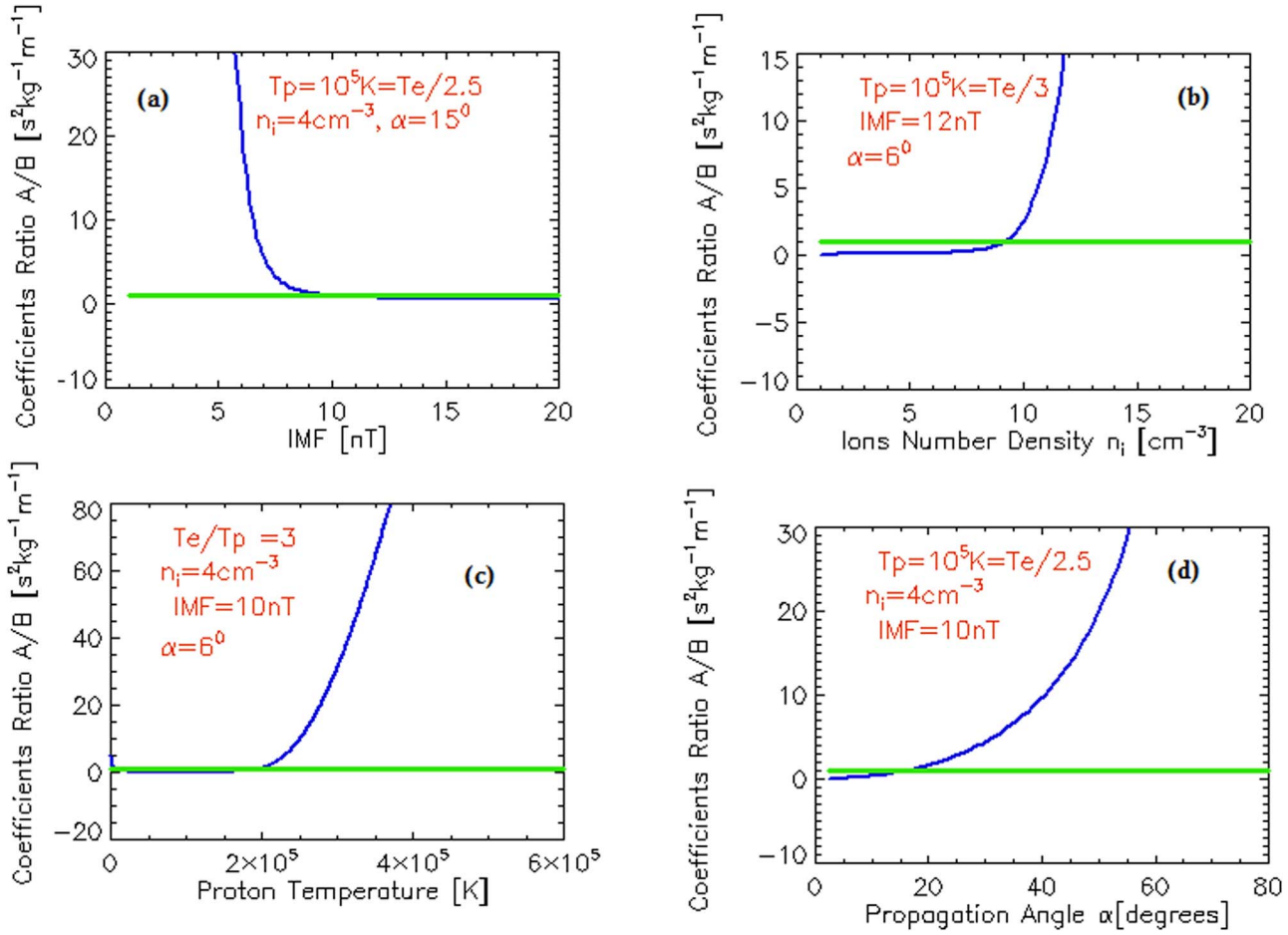

Figure 11. Effects of (a) interplanetary magnetic field (IMF), (b) ion number density n_i, (c) proton temperature, and (d) fast magnetosonic wave propagation angle on the ratio of convection to dispersion (A/B) coefficients of Equation (5).

is obvious from the overlapping of blue and green curves in Figure 11(c). Therefore, one can expect the formation of solitons at such temperatures. However, at high temperatures $T_p > 3 \times 10^5$ K, the ratio $A/B \gg 1$ and turbulence is most likely because wave steepening is dominant over wave spreading.

The effect of wave propagation angle (with respect to ambient magnetic field) on the coefficients ratio (A/B) of the KdV Equation (5) is shown in Figure 11(d). When propagation angle is less than 20° then A and B are comparable and soliton formation can be expected. However for high propagation angles (>40°) the convection coefficient is much greater than dispersion coefficient. Consequently, one can expect the evolution of turbulence for modes propagating at such high angles with respect to IMF.

The simulation results in Figures 6 and 8 which lead to single solitons are most appropriate for explaining the solar wind behavior in the presence of high IMF. The simulation results in Figures 7 and 10 are applicable to fast magnetosonic modes propagating with angles less than 10° with respect to IMF in solar wind plasma, in the presence of ions with number densities less than 8 cm^{-3}. The simulation results in Figure 9 are pertinent to explain the solar wind behavior in the presence of ejecta and at low IMF values where convection dominates the dispersion in solar wind.

Figures 12(a)–(d) present the power spectra (obtained by using an algorithm based on fast Fourier transform (FFT)) for IMF, its three components B_x, B_y, and B_z, respectively, during 2015 January 1–3. The turbulence in Figures 12(a)–(d) can be identified from simultaneous occurrence of wave bands in the 1–5 mHz frequency range. This indicates waves mixing at periods 200–1000 s. There are two types of regions in all panels of Figures 12(a)–(d). The regions of high (dark red regions at 8×10^{-5} $(nT)^2/Hz$) and low (blue regions at 2×10^{-5} $(nT)^2/Hz$) powers. Some time for the fixed frequency high and low power regions interchange each other temporally, which indicates power increase and decrease in the corresponding wave. Such changes in power can physically occur due to various mechanisms, possibly including wave–wave and wave–particle interactions. When a wave loses energy its power reduces to 2×10^{-5} $(nT)^2/Hz$. Contrarily, when a wave gains energy its power is increased. The rapid temporal changes in power for IMF (Figure 12(a)) are obvious at high frequencies (4–5 mHz) during 2015 January 1–3. The lower band (1–3 mHz) IMF turbulence is mostly at high powers except a few intervals where its power is reduced to 2×10^{-5} $(nT)^2/Hz$. For IMF (Figure 12(a)) and IMF–B_x (Figure 12(b)) components, the power associated with 1–3 mHz oscillations is greater than power contained in 3–5 mHz waves. The temporal evolution of IMF–B_y turbulence (Figure 12(c)) is distinctly different from those shown in Figures 12(a) and (b). Although the strongest power is associated with the lower frequencies (1–3 mHz) in IMF–B_z turbulence (Figure 12(d)) but the temporal evolution of

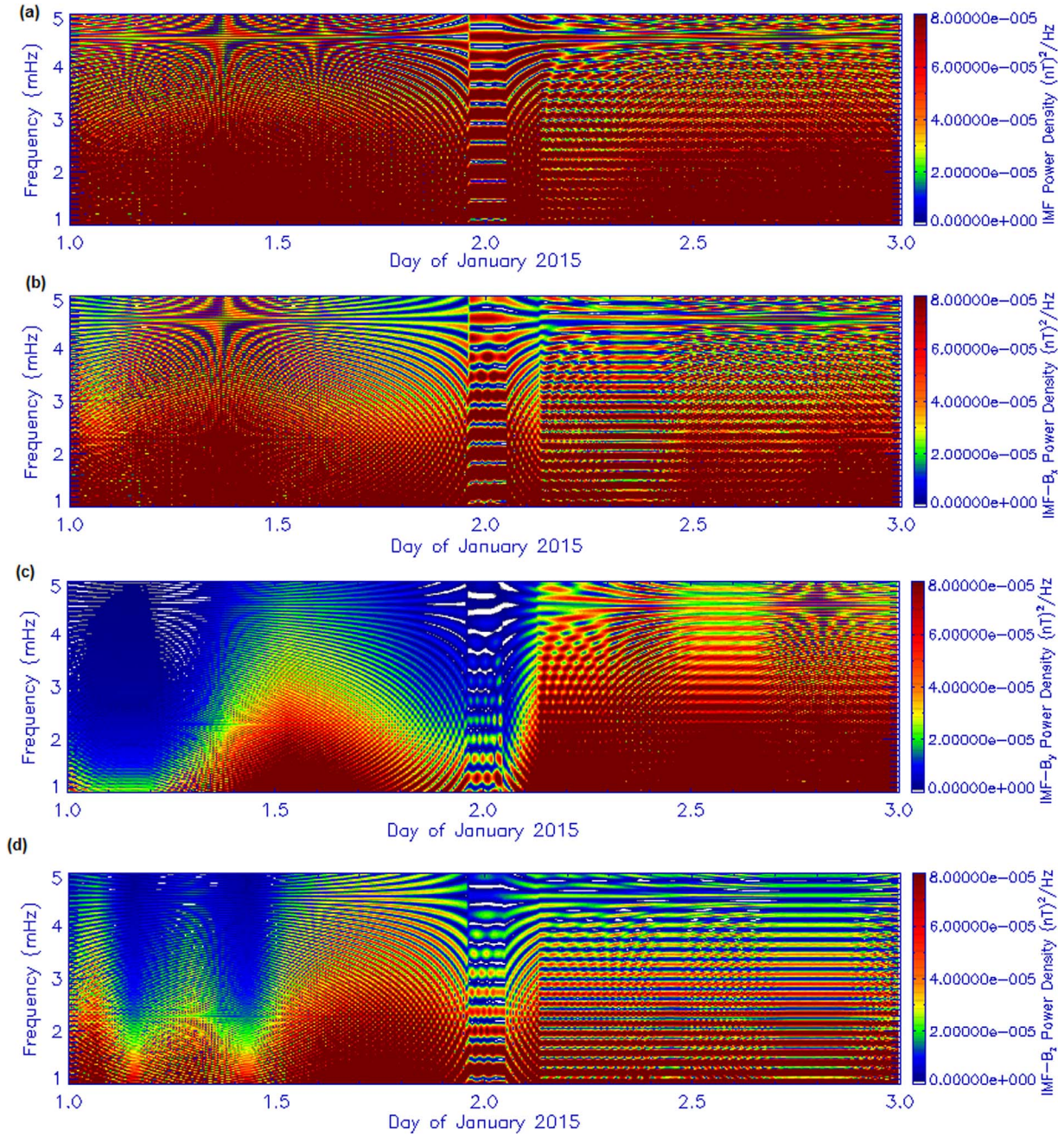

Figure 12. Dynamic power spectrum of (a) IMF, (b) IMF-Bx, (c) IMF-By, and (d) IMF-Bz during 2015 January 1–3. The spectrum is obtained by using an algorithm based on fast Fourier transform (FFT).

its power spectrum is entirely different from those presented in Figures 12(a)–(c).

7. Summary and Conclusions

This work is focused to explain the multi-satellite wave observations at 1 au during 2015 January 1–31. In the considered time interval multi-satellites observed single solitons, soliton trains, and turbulence in the IMF, solar wind speed, density, temperature, and dynamic pressure. The FDTD simulation results show that single soliton propagation occur in two circumstances: (a) when the system is initially perturbed by a weak shock wave and (b) when the ratio of dispersion to convection coefficients is 5. The soliton trains are developed when the system is excited by a strong shock and the convection coefficient is smaller than or equal to the dispersion coefficient. The simulation results support turbulence when the system is driven by stronger shock and nonlinear convection coefficient (A) exceeds the dispersion coefficient (B) in the considered convective and dispersive system. Using Hall MHD model for fast magnetosonic solitons, it is found that the ratio of convection to dispersion coefficients (A/B) is significantly affected by the solar wind plasma and magnetic field parameters. Specifically, at low IMF values $A/B \gg 1$, one expects the evolution of fast magnetosonic solitons into Alfvénic turbulence. However, at high IMF values the enhancement of the Hall term leads to $A/B = 1$ and consequently gives favorable conditions for soliton formation. These findings are found to be in good agreement with solar

wind data in the presence of shocks, sheath, ejecta, and MCs. It is also found that an increase in ion number density, proton temperature, and angle of propagation with ambient magnetic field all give $A/B \gg 1$ and lead to turbulence.

The authors acknowledge J.H. King, N. Papitashvili, cdaweb, and OMNI for the data.

References

Ballai, I., Thelen, J. C., & Roberts, B. 2003, A&A, 404, 701
Belashov, V. Y., & Vladimirov, S. V. 2005, Solitary Waves in Dispersive Complex Media: Theory, Simulation, Applications, Vol. 149 (Berlin: Springer)
Berezhiani, V. I., & Mahajan, S. M. 1994, PhRvL, 73, 1110
Boozer, A. H. 2005, RvMP, 76, 1071
Burch, J. L., Alexander, C. J., & Angelopoulos, V. 2004, Plasma Physics of the Local Cosmos (Washington, DC: The National Academies Press)
Burlaga, L., Sittler, E., Mariani, F., & arid Schwenn, R. 1981, JGRA, 86, 6673
Burlaga, L. F., Plunkett, S. P., & Cyr, O. C., St. 2002, JGRA, 107, 1266
Cattell, C., Dombeck, J., Wygant, J., et al. 2005, JGRA, 110, A01211
Cattell, C., Neiman, C., Dombeck, J., et al. 2003, NPGeo, 10, 13
De Vries, G., & Korteweg, D. J. 1895, PMag, 39, 422
Dungey, J. W. 1961, PhRvL, 6, 47
Echer, E., Gonzalez, W. D., & Tsurutani, B. T. 2008, GeoRL, 35, L06S06
Esirkepov, T., Nishihara, K., Bulanov, S. V., & Pegoraro, F. 2002, PhRvL, 89, 275002
Fränz, M., Horbury, T. S., Vincent Génot, O., et al. 2003, in AIP Conf. Proc. 679, Solar Wind Ten, ed. M. Velli, R. Bruno, & F. Malara (Melville, NY: AIP), 562
Goldstein, M. L. 2001, In Physics of Space: Growth Points and Problems (Dordrecht: Springer), 349
Goldstein, M. L., & Roberts, D. A. 1999, PhPl, 6, 4154
Goldstein, M. L., Roberts, D. A., & Matthaeus, W. H. 1995, ARA&A, 33, 283
Gonzalez, W. D., Joselyn, J. A., Kamide, Y., et al. 1994, JGRA, 99, 5771
Gonzalez, W. D., & Tsurutani, B. T. 1987, P&SS, 35, 1101
Gosling, J. T., & Pizzo, V. J. 1999, SSRv, 89, 21
Graham, D. B., Khotyaintsev, Y. V., Vaivads, A., & André, M. 2016, JGRA, 121, 3069
Gueroult, R., Ohsawa, Y., & Fisch, N. J. 2017, PhRvL, 118, 125101
Howard, T. 2011, Coronal Mass Ejections: An Introduction, Vol. 376 (Berlin: Springer)
Hundhausen, A. J., Burkepile, J. T., St., & Cyr, O. C. 1994, JGR, 99, 6543
Hutchinson, J. A., Wright, D. M., & Milan, S. E. 2011, JGRA, 116, A09211
Jian, L. K., Russell, C. T., Luhmann, J. G., Skoug, R. M., & Steinberg, JTz. 2008, SoPh, 249, 85
Kilpua, E., Koskinen, H. E., & Pulkkinen, T. I. 2017a, LRSP, 14, 5
Kilpua, E. K. J., Balogh, A., von Steiger, R., & Liu, Y. D. 2017b, SSRv, 212, 1271
Koskinen, H. 2011, Physics of Space Storms from the Solar Surface to the Earth (Berlin: Springer)
Koskinen, H. E. J., & Huttunen, K. Ej. 2006, SSRv, 124, 169
Kumar, A., Shukla, C., Verma, D., Das, A., & Kaw, P. 2019, PPCF, 61, 065009
Lontano, M., Passoni, M., & Bulanov, S. V. 2003, PhPl, 10, 639
Matsumoto, H., Deng, X. H., Kojima, H., & Anderson, R. R. 2003, GeoRL, 30, 1326
Mjolhus, E., & Hada, Tohru. 1997, in Nonlinear Waves and Chaos in Space Plasmas, ed. T. Hada & H. Matsumoto (Tokyo: Terra Scientific Publishing Company), 121
Mozer, F. S., Agapitov, O. V., Artemyev, A., et al. 2015, GeoRL, 42, 3627
Ohsawa, Y. 2017, PhPl, 24, 112304
Ohsawa, Y. 2018, PhPl, 25, 052305
Ovenden, C. R., Shah, H. A., & Schwartz, S. J. 1983, JGRA, 88, 6095
Patel, V. L., & Dasgupta, B. 1987, PhyD, 27, 387
Pokhotelov, O. A., Pokhotelov, D. O., Gokhberg, M. B., et al. 1996, JGRA, 101, 7913
Popel, S. I., Golub, A. P., Losseva, T. V., et al. 2003, PhRvE, 67, 056402
Richardson, I. G., & Cane, H. V. 2011, SpWea, 9, S07005
Richardson, I. G., Cliver, E. W., & Cane, H. V. 2000, JGR, 105, 18,203
Shatashvili, N. L., Javakhishvili, J. I., & Kaya, H. 1997, Ap&SS, 250, 109
Stasiewicz, K. 2004, PhRvL, 93, 125004
Stasiewicz, K., Shukla, P. K., Gustafsson, G., et al. 2003, PhRvL, 90, 085002
Stawarz, J. E., Ergun, R. E., & Goodrich, K. A. 2015, JGRA, 120, 1845
Taflove, A., & Hagness, S. C. 2005, Computational Electrodynamics: The Finite-difference Time-domain Method (Boston, MA: Artech House Publishers)
Treumann, R. A., & Baumjohann, W. 1997, Advanced Space Plasma Physics, Vol. 30 (London: Imperial College Press)
Tsurutani, B. T., Gonzalez, W. D., Gonzalez, A. L., et al. 2004, SSRv, 111, 267
Williams, J. D., Chen, L.-J., Kurth, W. S., Gurnett, D. A., & Dougherty, M. K. 2006, GeoRL, 33, L06103
Yermolaev, Yu I., Lodkina, I. G., Nikolaeva, N. S., Yu Yermolaev, M., & Riazantseva, M. O. 2017, CosRe, 55, 178
Yermolaev, Yu I., Nikolaeva, N. S., Lodkina, I. G., & Yermolaev, M. Yu. 2009, CosRe, 47, 81
Yoshizawa, A., Itoh, S. I., & Itoh, K. 2002, Plasma and Fluid Turbulence: Theory and Modelling (Boca Raton, FL: CRC Press)